

# Non-virialised clusters for detection of Dark Energy–Dark Matter interaction

M. Le Delliou<sup>1,2\*</sup>, R. J. F. Marcondes<sup>2\*</sup>, G. B. Lima Neto<sup>3\*</sup> and E. Abdalla<sup>2\*</sup>

<sup>1</sup>*Instituto de Física Teórica – Universidade Estadual Paulista, R. Dr. Bento Teobaldo Ferraz, 271 - Bloco II, Barra-Funda CEP 01140-070 - São Paulo, SP, Brazil*

<sup>2</sup>*Departamento de Física Matemática – Instituto de Física – Universidade de São Paulo, Rua do Matão Travessa R Nr.187 CEP 05508-090, São Paulo/SP, Brazil*

<sup>3</sup>*Instituto de Astronomia, Geofísica e Ciências Atmosféricas, Universidade de São Paulo, Rua do Matão 1226, Cidade Universitária, CEP 05508-090, São Paulo/SP, Brazil*

Send offprint requests to: MLeD  
Accepted ... Received ...; in original form ...

## ABSTRACT

In a  $\Lambda$ CDM universe it is expected that clusters of galaxies are not in equilibrium. In this work, we investigate the possibility to evaluate the departure from virial equilibrium in order to detect, in that balance, effects from a Dark matter–Dark energy interaction. We continue, from previous works, using a simple model of interacting dark sector, the Layzer–Irvine equation for dynamical virial evolution, and employ optical observations in order to obtain the mass profiles through weak lensing and X-ray observations giving the intracluster gas temperatures. Through a Monte Carlo method, we generate, for a set of clusters, measurements of observed virial ratios, interaction strength, rest virial ratio and departure from equilibrium factors. We found a compounded interaction strength of  $-1.61^{+2.23}_{-16.34}$ , compatible with no interaction, but also a compounded rest virial ratio of  $-0.78 \pm 0.13$ , which would entail a  $2\sigma$  detection. We confirm quantitatively that clusters of galaxies are out of equilibrium but further investigation is needed to constrain a possible interaction in the dark sector.

**Key words:** Cosmology: theory, dark matter, dark energy, large-scale structure of Universe – Galaxies: clusters: general – Gravitation – X-rays: galaxies: clusters.

## 1 INTRODUCTION

The surprising result of cosmological accelerated expansion, discovered at first from supernovae data (Perlmutter et al. 1998), and the long sought Dark Matter seen around clumped matter (Zwicky 1933, 1937), found their importance combined and confirmed by the results of Cosmological Microwave Background observations. This leads to the fair confidence on the existence of a Dark sector, composed by an inert Cold Dark Matter accounting for  $\sim 23\%$  of the Universe and a rather mysterious Dark Energy, accelerating the cosmos, accounting for a noter  $\sim 72\%$  (Hinshaw et al. 2013; Bennett et al. 2013).

The nature of these components is largely unknown. Several candidates for Dark Matter appeared in the literature, with no preference from observations. For Dark Energy, a cosmological constant (de Sitter space type) is the usual observationally preferred choice and forms the basis of the so-called standard, or concordance, cosmology (Hinshaw et al. 2013; Bennett et al. 2013; Aghanim et al. 2012; Ade et al. 2013).

However, such cosmological constant is an awful choice from the theoretical point of view: it has been argued that it differs by 120 orders of magnitude from a reasonable field theory estimation (Weinberg 1989, 2008). From observations, the fact that its energy density is of the same order of magnitude today as the Dark Matter is a mystery: both depend on cosmological time in a completely different way, leading to the so-called coincidence problem (Amendola 2000; Tocchini-Valentini & Amendola 2002; Zimdahl & Pavón 2001, 2003).

From the observational standpoint it turns out to be very difficult to distinguish a clear departure from the standard cosmological model. Indeed, cosmology is reasonably well described by a positive cosmological constant in a framework of a set of Einstein equations. A redshift dependent equation of state of Dark Energy is possible but the error bars obtained from observations so far are still consistent (to one or two standard deviations) with the standard cosmological model, although such model is theoretically disfavoured as discussed above.

On the contrary, dynamic Dark Energy was theoretically introduced in attempts to solve the fine tuning and coincidence problems described above (Wetterich 1988; Ratra & Peebles 1988). In this framework, it was pointed out that, since the main components of

\* Email: delliou@ift.unesp.br (MLeD); mrafael@if.usp.br (RJFM); gas-tao@astro.iag.usp.br (GBLN); eabdalla@if.usp.br (EA)

the universe in the standard cosmological models are yet unknown, that dark sector interactions, that is the non-minimal coupling between Dark Matter and Dark Energy, would be the most natural model to consider (Amendola 2000). Such models are not ruled out by observations.

One possibility that has been put forward a few years ago is that interaction can spoil the virial theorem (or else the Layzer–Irvine equation in General Relativity) (Bertolami et al. 2007; Le Delliou et al. 2007; Bertolami et al. 2008, 2009, 2012). Such a possibility has been checked by different groups (Abdalla et al. 2009, 2010; He et al. 2010) and the results are still not completely settled, although there seems to be a reasonable possibility of an interacting dark sector. Indeed, using a series of data from clusters, we can infer, under some not too severe conditions, whether Dark Energy can play the role of a hidden external driving force by means of the dark sector interaction and thus apparently spoil the virial theorem leaving a trace of the would-be interaction. In such a case, some limits on the interaction can be obtained.

In this paper we consider the virial condition and investigate if it can be clearly imposed observationally, by enquiring into cluster data and their corresponding observations in the optical and X-ray bands. These bands were chosen because, from deep optical imaging it is possible to derive the total mass distribution through weak-lensing effect of background galaxies, and from x-ray observations we can determine the density and temperature of the intracluster gas, which traces the cluster gravitational potential well.

In previous papers, deviations from the virial theorem, as described in the Layzer–Irvine equation, were searched in very relaxed clusters (Bertolami et al. 2007; Le Delliou et al. 2007; Bertolami et al. 2008, 2009, 2012) or in large sets of clusters (Abdalla et al. 2009, 2010; He et al. 2010). In Bertolami et al. (2007), optical (weak lensing) and X-rays data were used to provide the first hint of a detection of a putative violation of the Equivalence Principle in the virial state of Abell 586. Subsequent works aimed at refining the method on Abell 586 (Le Delliou et al. 2007; Bertolami et al. 2008, 2009) and introduced another relaxed cluster candidate (Abell 1689, Bertolami et al. 2012). In Abdalla et al. (2009), optical and X-ray data were compared and a hint of systematic bias in the estimation of masses, if the usual virial conditions are employed, was found. In a subsequent paper (Abdalla et al. 2010), the work was extended to a larger set of clusters. In both cases, it was argued that such signals might point to new physics to be uncovered and more specifically to a correction of the virial theorem due to a would-be interaction of Dark Matter with a hidden sector, i.e. dark energy, driving the system away from the virial equilibrium.

In the present work, we address some of these issues raised previously, digging into the internal structure of the clusters, in order to find, in a very direct way, not only the kinetic versus potential energy — the virial ratio — from each system (cluster), but also to use the full dynamics of the Layzer–Irvine equation in order to extract an assessment of the departure from self-gravitating equilibrium.

The next Section 2 describes the techniques used for extracting relevant dynamical quantities from the data. Section 3 compiles the relevant data and summarises their treatment. The results obtained are given in Section 4, and we conclude with a discussion in Section 5. We adopt whenever necessary the standard  $\Lambda$ CDM parameters:  $\Omega_M = 0.27$  for the Matter density parameter,  $\Omega_{DE} = 0.73$  for the Dark Energy parameter and Hubble constant  $H_0 = 73.8 \text{ km s}^{-1} \text{ Mpc}^{-1}$ .

## 2 VIRIAL RATIO AND DEPARTURE FROM EQUILIBRIUM FOR NON-VIRIALISED CLUSTERS

In Abdalla et al. (2009), a model of interaction involving the coupling of both Dark Matter (DM) and Dark Energy (DE) was introduced for which the Layzer–Irvine equation was deduced. We adopt a form, in what follows, that is inspired by such model.

### 2.1 The Layzer–Irvine model with interaction

The Layzer–Irvine equation (Peebles 1993) is a model of dynamical virial balance where the disturbance is simplified in the expansion of the background universe.

#### 2.1.1 The interaction model

Following Abdalla et al. (2009, 2010) and He et al. (2010), we model the DM–DE interaction via a heat flux between the two species in their partial Bianchi identities in a Friedmann–Lemaître–Robertson–Walker (FLRW) background model

$$\dot{\rho}_{DM} + 3H\rho_{DM} = 3H(\xi_1\rho_{DM} + \xi_2\rho_{DE}), \quad (1)$$

$$\dot{\rho}_{DE} + 3H\rho_{DE}(1 + \omega_{DE}) = -3H(\xi_1\rho_{DM} + \xi_2\rho_{DE}). \quad (2)$$

Here we have used the indices to refer to species, the couplings  $\xi_1$  and  $\xi_2$ , hereafter interaction strengths, the densities denoted by  $\rho_x$  while their corresponding equation of state reads  $\omega_x$  and the FLRW Hubble parameter  $H$ . In what follows we shall simplify the interaction by choosing  $\xi_1 = \frac{\xi}{18}$  and  $\xi_2 = -\frac{\xi}{6} \frac{\rho_{DM}}{\rho_{DE}}$  and writing  $\rho_{DM} = \rho$ , yielding a positive flux  $\frac{\xi}{3}H\rho$  towards DE when all terms are positive.

The resulting Layzer–Irvine equation for the DM component (He et al. 2010), referring to its kinetic energy density with  $\rho_K$  while its potential energy density writes  $\rho_W$ , reads

$$\dot{\rho} + H \left[ \left( 2 - \frac{\xi}{3} \right) \rho_K + \left( 1 - \frac{\xi}{3} \right) \rho_W \right] = 0. \quad (3)$$

In case of equilibrium, the time derivative vanishes and yield the interacting virial balance as

$$\frac{\rho_K}{\rho_W} = -\frac{1 - \frac{\xi}{3}}{2 - \frac{\xi}{3}}. \quad (4)$$

However, in this work, we want to take into account departures from equilibrium.

Note that certainty of convergence of the energy density towards equilibrium, together with other magnitude restriction considerations (e.g. He et al. 2011), prescribes from Eq. (3) to exclude values of  $\xi$  higher than 3.

#### 2.1.2 The Non-Virialised model

In order to simplify the calculation, we approximate the departure of  $\rho_K$  from balance as proportional to the departure of  $\rho_W$  and introduce Eq. (4) into (3) to get

$$\left[ 1 - \frac{1 - \frac{\xi}{3}}{2 - \frac{\xi}{3}} \right] \dot{\rho}_W = -H \left[ \left( 2 - \frac{\xi}{3} \right) \rho_K + \left( 1 - \frac{\xi}{3} \right) \rho_W \right] \quad (5)$$

so

$$\frac{\rho_K}{\rho_W} = -\frac{1 - \frac{\xi}{3}}{2 - \frac{\xi}{3}} - \frac{1}{\left( 2 - \frac{\xi}{3} \right)^2} \frac{\dot{\rho}_W}{H\rho_W}. \quad (6)$$

Here we find that the true virial balance (4) is corrected by a term we call departure from equilibrium. For our approximation (4) to remain valid, the DM halo has to be close to virial balance, so we have to check that

$$\left| \frac{\dot{\rho}_W}{H\rho_W} \right| \ll \left( 2 - \frac{\xi}{3} \right) \left( 1 - \frac{\xi}{3} \right). \quad (7)$$

In that case,  $\rho_K$ ,  $\rho_W$ ,  $\dot{\rho}_W$  and  $H$  being observable, we can solve Eq. (6) for the coupling and obtain

$$\xi = 3 \left( \frac{3 + 4 \frac{\rho_K}{\rho_W} - \sqrt{1 - \frac{4\dot{\rho}_W}{H\rho_W} \left( 1 + \frac{\rho_K}{\rho_W} \right)}}{2 \left( 1 + \frac{\rho_K}{\rho_W} \right)} \right). \quad (8)$$

The expression verifies the classical, non-interacting and virialised, result:  $\xi = 0$  for  $\dot{\rho}_W = 0$  and  $\frac{\rho_K}{\rho_W} = -\frac{1}{2}$ . Note that this equation is singular at  $\frac{\rho_K}{\rho_W} = -1$ , which originates in the left-hand side of Eq. (5) and corresponds to infinite  $\xi$ . We now need to evaluate  $\rho_K$ ,  $\rho_W$ ,  $\dot{\rho}_W$  and  $H$  from cluster observations. However, as we will see in Section 2.2.3, the departure from equilibrium factor  $\frac{\dot{\rho}_W}{H\rho_W}$  is not a pure observable and depends on  $\xi$ .

## 2.2 The evaluation from clusters

Cosmologically interesting observations of clusters are produced in many surveys and studies such as Okabe et al. (2010) and Aghanim et al. (2012). In order to maximise our sample, while being able to separately evaluate from observations the kinetic and potential energy states of each cluster, we have restricted inputs to weak lensing Navarro, Frenk and White (NFW) fit parameters (Navarro et al. 1996), X-ray derived  $c_{500}$  NFW fits, assuming hydrostatic equilibrium, and X-ray temperatures.

### 2.2.1 The NFW density and Weak Lensing mass

The NFW density profile (Navarro et al. 1996) found in  $N$ -body simulations is commonly used to fit observed clusters in order to parametrize their mass distribution. The classical form of the NFW profile involves the radius of logarithmic slope change  $r_0$  and the corresponding density  $\rho_0$ . Assuming the virial radius of clusters lies at a density contrast of about 200 above the background density for clusters, the NFW concentration parameter can be defined as  $c = \frac{r_{200}}{r_0}$ . Moreover, the profile's integration yields a mass profile from which  $M_{200}$  can be extracted. In terms of  $c$ ,  $r_{200}$  and  $M_{200}$ , the mass and density profiles read

$$M = \frac{M_{200}}{\ln(1+c) - \frac{c}{1+c}} \left[ \ln \left( 1 + c \frac{r}{r_{200}} \right) - \frac{c \frac{r}{r_{200}}}{1 + c \frac{r}{r_{200}}} \right], \quad (9)$$

$$\rho = \frac{M_{200}}{4\pi r_{200}^3 \left[ \ln(1+c) - \frac{c}{1+c} \right]} \frac{c^2}{\frac{r}{r_{200}} \left( 1 + c \frac{r}{r_{200}} \right)^2}. \quad (10)$$

The parameter describing the best-fit NFW profile,  $c$  and  $r_{200}$  (or  $M_{200}$ ), can be obtained from the mass reconstruction technique, which requires deep imaging with small point-spread-function (PSF) that can detect the weak lensing effect.

### 2.2.2 The potential and kinetic energy density evaluations

With the previously presented NFW mass profile, the density of potential energy is straightforwardly integrated

$$\begin{aligned} \rho_W &\equiv -\frac{4\pi}{4\pi r_{200}^3/3} \int_0^{r_{200}} \frac{\rho(r)GM(r)}{r} r^2 dr \\ &= -\frac{3GM_{200}^2}{4\pi r_{200}^4 f_c}, \end{aligned} \quad (11)$$

$$\text{with } f_c \equiv \frac{(1+c) \left[ \ln(1+c) - c(1+c)^{-1} \right]^2}{c \left[ \frac{1}{2} \left\{ (1+c) - (1+c)^{-1} \right\} - \ln(1+c) \right]}. \quad (12)$$

On the other hand, in order to evaluate the kinetic state of the cluster, we use published X-rays observations, where we just need to obtain the X-ray temperature to get the equipartition formula

$$\rho_K = \frac{3}{2} N \frac{kT_X}{V} = \frac{9}{8\pi} \frac{M_{200}}{r_{200}^3} \frac{kT_X}{\mu m_H}, \quad (13)$$

gauging the equivalent number of particles from the total mass given by weak lensing  $\frac{M_{200}}{\mu m_H}$ , where  $\mu$  is the mean molecular mass in the intracluster gas and  $m_H$  is the mass of a proton. The advantage of this method, compared, say, to using the galaxy velocity dispersion or a scaling relation  $\sigma_X - T_X$ , as in Bertolami et al. (2007), Le Delliou et al. (2007) and Bertolami et al. (2008, 2009, 2012), is that we avoid the error from the scatter in the scaling relation. We are justified in evaluating the kinetic state of clusters through the single compounded temperature  $T_X$ , extracted from the X-ray flux of the whole  $r_{500}$  central region, as it already largely encompasses the turnaround of the temperature profile (Vikhlinin et al. 2005; Pratt et al. 2007; Moretti et al. 2011), and therefore represents well the total density averaged temperature (the so-called virial temperature).

At this point the virial ratio can be evaluated as

$$\frac{\rho_K}{\rho_W} = -\frac{3}{2} \frac{r_{200}}{GM_{200}} \frac{kT_X}{\mu m_H} f_c. \quad (14)$$

### 2.2.3 The virial and departure from equilibrium evaluation

The departure from equilibrium factor can be rewritten as

$$-\frac{1}{\left( 2 - \frac{\xi}{3} \right)^2} \frac{\dot{\rho}_W}{H\rho_W} = -\frac{1}{\left( 2 - \frac{\xi}{3} \right)^2} \frac{\rho'_W}{H\rho_W} \dot{r}_{200}, \quad (15)$$

where we get from Eq. (11)

$$\begin{aligned} \frac{d \ln(-\rho_W)}{dr_{200}} &= \frac{\rho'_W}{\rho_W} \\ &= \frac{(cg_c - 3)}{r_{200}} \end{aligned} \quad (16)$$

$$\text{with } g_c \equiv \frac{\ln(1+c) - c(1+c)^{-1}}{\frac{c}{2}(c+2) - (1+c)\ln(1+c)}. \quad (17)$$

Now remains to evaluate  $\dot{r}_{200}$ . We can define the kinetic density using a one dimensional velocity dispersion, thus defining  $\sigma_X^2$ :

$$\rho_K = \frac{3}{2} \frac{M_{200}}{V} \sigma_X^2 \Rightarrow \sigma_X^2 = \frac{kT_X}{\mu m_H}. \quad (18)$$

We now define the theoretical average velocity dispersion the cluster would have if it were at virial equilibrium, adiabatically evolving from the current state (meaning keeping potential energy about

constant)

$$\left(\frac{\rho_K}{\rho_W}\right)_{th} = -\frac{1 - \frac{r}{3r_{th}}}{2 - \frac{r}{3r_{th}}} \text{ with } \rho_{Kth} = \frac{3}{2} \frac{M_{200}}{V} v_{th}^2 \quad (19)$$

$$\Leftrightarrow v_{th}^2 = \frac{1}{3} \frac{6 - 2\xi}{6 - \xi} \frac{GM_{200}}{f_c r_{200}}. \quad (20)$$

We can finally evaluate the time evolution of  $r_{200}$  by taking its difference with the velocity dispersion

$$\dot{r}_{200} = \sqrt{\sigma_X^2} - \sqrt{v_{th}^2} = \sigma_X - v_{th}, \quad (21)$$

we obtain

$$-\frac{\dot{\rho}_W}{H\left(2 - \frac{\xi}{3}\right)^2 \rho_W} = -\frac{1}{H\left(2 - \frac{\xi}{3}\right)^2} \frac{(c g_c - 3)}{r_{200}} \times \left( \sqrt{\frac{kT_X}{\mu m_H}} - \sqrt{\frac{1}{3} \frac{6 - 2\xi}{6 - \xi} \frac{GM_{200}}{f_c r_{200}}} \right). \quad (22)$$

The departure from equilibrium presented here is model-dependent; however the method can use any model we want that gives a definite shift to the virial balance.

### 3 COMPUTATIONS OF THE VIRIAL RATIOS AND DEPARTURE FROM EQUILIBRIUM FOR A SET OF NON-VIRIALISED CLUSTERS

#### 3.1 The sample

We selected a sample of 14 clusters whose NFW parameters are given in the literature. We have best-fit virial masses  $M_{vir}$  and concentration parameters  $c_{vir}$  for the NFW model and masses  $M_{200}$  estimated from this three-dimensional model fitting for the clusters A209, A267, A383, A521, A1835, A2219, A2261, A2390, A2631 and A586 (Okabe et al. 2010); and weak lensing masses  $M_{500}$  and best fitting X-ray NFW concentration parameter  $c_{500}$  for the clusters A520, A963, A1914 and A2034 (Aghanim et al. 2012). The spectroscopically determined temperatures  $T_X$ , given in Aghanim et al. (2012), are measured within  $r_{500}$ . Uncertainties correspond to  $1\sigma$  confidence level (C.L.). Errors in redshifts (Aghanim et al. 2012) are not specified but can be safely neglected compared to the errors in other quantities (the typical spectroscopic redshift error is around 1%).

##### 3.1.1 Uniforming the NFW profiles

We want to have all NFW profiles parametrised by  $M_{200}$  and  $c$ . In general, within a radius  $r_\Delta$ , i.e., the scale for which the density is equal to  $\Delta$  times the critical density, we have

$$\Delta = \frac{M_\Delta}{\frac{4}{3} \pi r_\Delta^3 \rho_c(z)}, \quad (23)$$

which results in an expression for the radius given the mass:

$$r_\Delta = \frac{1}{H(z)} \sqrt[3]{\frac{2GM_\Delta H(z)}{\Delta}}. \quad (24)$$

For the latter set of clusters, with NFW profiles specified by  $M_{500}$  and  $c_{500} = \frac{r_{200}}{r_0}$  (rather than  $c_{200}$ , which we called just  $c$ ), the parameter  $r_0 = \frac{r_{200}}{c} = \frac{r_{500}}{c_{500}}$  comes immediately by using Eq. (24) for  $\Delta = 500$ . Using SYMPY in python, we get  $M_{200}$  and  $r_{200}$  by solving simultaneously an equation similar to (9) (but parametrized

by  $M_{500}$  and  $c_{500}$  and evaluated at  $r_{200}$  to give  $M_{200}$ ) and Eq. (24) with  $\Delta = 200$

$$\begin{cases} M_{200} = \frac{M_{500}}{\ln(1 + c_{500}) - \frac{c_{500}}{1 + c_{500}}} \times \\ \quad \times \left[ \ln\left(1 + c_{500} \frac{r_{200}}{r_{500}}\right) - \frac{c_{500} \frac{r_{200}}{r_{500}}}{1 + c_{500} \frac{r_{200}}{r_{500}}} \right], \\ r_{200} = \frac{1}{H(z)} \sqrt[3]{\frac{GM_{200} H(z)}{100}}. \end{cases} \quad (25)$$

Then we can finally compute  $c = \frac{r_{200}}{r_0}$ .

For the former set, with NFW profiles specified by  $M_{200}$ ,  $M_{vir}$  and  $c_{vir}$ , ‘‘vir’’ would correspond to some  $\Delta_{vir}$  around 200 but this value can vary with the redshift. Then we proceed as follows. We compute  $r_{200}$  from Eq. (24) and solve

$$M_{200} = \frac{M_{vir}}{\ln(1 + c_{vir}) - \frac{c_{vir}}{1 + c_{vir}}} \times \left[ \ln\left(1 + c_{vir} \frac{r_{200}}{r_{vir}}\right) - \frac{c_{vir} \frac{r_{200}}{r_{vir}}}{1 + c_{vir} \frac{r_{200}}{r_{vir}}} \right] \quad (26)$$

for  $r_{vir}$ .  $\Delta_{vir}$  can also be determined now with  $r_{vir}$  and  $M_{vir}$ , inverting Eq. (24). Finally, we have  $r_0 = \frac{r_{vir}}{c_{vir}}$  and  $c = \frac{r_{200}}{r_0}$ . With  $c$  and  $M_{200}$ , we can now proceed to the computation of the virial ratios.

#### 3.2 Monte Carlo estimation of errors

We apply a Monte Carlo method to propagate uncertainties through the numerical solutions. We perform multiple realisations of each cluster, with the observables assuming values that are drawn from a distribution which reflects the  $1\sigma$  confidence intervals from the original asymmetrical uncertainties. We then carry the computations for all the realisations of each cluster and analyse the final distribution of the quantities of interest to get their error bars. In addition we introduce two selection criteria that we apply to the values of the interaction strength obtained with this method to conserve realisations: one physical, discussed in Sec. 2.1.1, selects  $\xi \leq 3$ , while the other avoids numerical problems, discussed in Sec. 2.1.2, by keeping only  $\xi \geq -200$  (see discussion in Sec. 4.2).

##### 3.2.1 Non-negative observables

Our input observables — mass, concentration and temperature — are always positive. To guarantee that their uncertainties will not lead to negative values in any of the random realisations, we choose a non-negative probability distribution whose probability density function (PDF) and cumulative distribution function (CDF) have simple analytical forms: the log-logistic distribution. Its PDF with parameters  $(\alpha, \beta)$  is

$$f_X(x; \alpha, \beta) = \frac{\frac{\beta}{\alpha} \left(\frac{x}{\alpha}\right)^{\beta-1}}{\left[1 + \left(\frac{x}{\alpha}\right)^\beta\right]^2} \quad (27)$$

and the CDF is given by

$$F_X(x; \alpha, \beta) = \frac{1}{1 + \left(\frac{x}{\alpha}\right)^\beta} \quad (28)$$

For a given observable  $X$  with measured value  $x_{-\Delta}^{+\Delta x_1}$ , we would like the Monte Carlo generating distribution to match the following criteria:

**Table 1.** Weak lensing masses  $M_{200}$ ,  $M_{\text{vir}}$  and concentration  $c_{\text{vir}}$  for the first subset of clusters. Masses are in units of  $h^{-1}10^{14}M_{\odot}$ .

Cluster	$M_{200}$	$M_{\text{vir}}$	$c_{\text{vir}}$
A209	$10.62^{+2.17}_{-1.81}$	$14.00^{+3.31}_{-2.60}$	$2.71^{+0.69}_{-0.60}$
A267	$3.23^{+0.82}_{-0.69}$	$3.85^{+1.08}_{-0.88}$	$6.00^{+2.11}_{-1.58}$
A383	$3.11^{+0.88}_{-0.69}$	$3.62^{+1.15}_{-0.86}$	$8.87^{+5.22}_{-3.05}$
A521	$4.58^{+1.00}_{-0.88}$	$5.85^{+1.45}_{-1.22}$	$3.06^{+1.01}_{-0.79}$
A586	$6.29^{+2.26}_{-1.69}$	$7.37^{+2.89}_{-2.08}$	$8.38^{+3.52}_{-2.52}$
A1835	$10.86^{+2.53}_{-2.08}$	$13.69^{+3.65}_{-2.86}$	$3.35^{+0.99}_{-0.79}$
A2219	$7.75^{+1.89}_{-1.60}$	$9.11^{+2.54}_{-2.06}$	$6.88^{+3.42}_{-2.16}$
A2261	$7.97^{+1.51}_{-1.31}$	$9.49^{+2.01}_{-1.69}$	$6.04^{+1.71}_{-1.31}$
A2390	$6.92^{+1.50}_{-1.29}$	$8.20^{+1.93}_{-1.63}$	$6.20^{+1.53}_{-1.28}$
A2631	$4.54^{+0.89}_{-0.78}$	$5.24^{+1.15}_{-0.98}$	$7.84^{+3.54}_{-2.28}$

Data from Okabe et al. (2010).

**Table 2.** Weak lensing masses  $M_{500}$  and X-ray concentration  $c_{500}$  for the second subset of clusters. Masses are in units of  $h^{-1}10^{14}M_{\odot}$ .

Cluster	$M_{500}$	$c_{500}$
A520	$3.0^{+0.8}_{-0.9}$	$0.5 \pm 0.2$
A963	$3.0^{+0.7}_{-0.5}$	$3.1 \pm 0.4$
A1914	$3.5^{+1.3}_{-1.4}$	$3.4 \pm 0.3$
A2034	$3.8^{+1.6}_{-1.8}$	$1.3 \pm 0.2$

Data from Aghanim et al. (2012).

- (i) The maximum probability coincides with the nominal measure;
- (ii) The probability of  $X$  lying between  $x - \Delta x_2$  and  $x + \Delta x_1$  is 68%;
- (iii) The PDF has the same value at the two points  $x - \Delta x_2$  and  $x + \Delta x_1$ , so that the interval in condition (ii) corresponds to the 68% most probable values, i.e.,  $1\sigma$  C.L.

In the case of the log-logistic distribution, these conditions are translated by:

- (i)  $\alpha \left( \frac{\beta-1}{\beta+1} \right)^{1/\beta} = x$  (for  $\beta > 1$ );
- (ii)  $F_X(x + \Delta x_1; \alpha, \beta) - F_X(x - \Delta x_2; \alpha, \beta) = 0.68$ ;
- (iii)  $f_X(x - \Delta x_2; \alpha, \beta) = f_X(x + \Delta x_1; \alpha, \beta)$ .

But these are too many conditions for a distribution which has only two parameters. We choose to relax condition (i) and solve (ii) and (iii) for  $\alpha$  and  $\beta$ . In practice our resulting maximum probabilities usually happen to be very close to  $x$ .

We use this approach in the error estimation for  $M_{200}$  and  $c$  from Sec. 3.1.1. After generating distributions for  $M_{500}$  and  $c_{500}$  or  $M_{\text{vir}}$ ,  $c_{\text{vir}}$  and  $M_{200}$  with their errors, shown in Tables 1 and 2, we take the opposite direction and get a best-fit log-logistic PDF for the distributions of  $M_{200}$  and  $c$ , now solving (ii) and (iii) for  $x - \Delta x_2$  and  $x + \Delta x_1$ . We assign the maximum probability of the distribution to the nominal value  $x$ . In Table 3 we summarize the data used for computation of the virial ratios and interaction according to the steps in Section 2.2.

### 3.2.2 General distribution fitting

A quantity  $Y$  which in principle can be positive or negative, like the interaction strength or the departure from equilibrium, as we will see in Sec. 4, can be difficult to fit in a log-logistic shape. For these

**Table 3.** Redshift, temperature and compiled NFW parameters of the 14 galaxy clusters. Temperatures are given in keV and masses in units of  $h^{-1}10^{14}M_{\odot}$ .

Cluster	$z$	$k_B T_X$	$M_{200}$	$c$
A1835	0.253	$8.4 \pm 0.1$	$10.86^{2.53}_{-2.08}$	$2.34^{+1.26}_{-0.92}$
A1914	0.171	$8.5 \pm 0.2$	$4.1^{+2.8}_{-1.9}$	$4.92^{+1.4}_{-0.91}$
A209	0.206	$6.6 \pm 0.2$	$10.62^{+2.17}_{-1.81}$	$1.87^{+0.78}_{-0.60}$
A2034	0.113	$6.4 \pm 0.2$	$4.5^{+5.0}_{-2.8}$	$1.97^{+0.60}_{-0.50}$
A2219	0.228	$9.6^{+0.3}_{-0.2}$	$7.75^{+1.89}_{-1.60}$	$4.51^{+4.04}_{-2.48}$
A2261	0.224	$6.1^{+0.6}_{-0.5}$	$7.97^{+1.51}_{-1.31}$	$4.34^{+2.40}_{-1.74}$
A2390	0.231	$9.1 \pm 0.2$	$6.92^{+1.50}_{-1.29}$	$4.31^{+2.50}_{-1.79}$
A2631	0.278	$7.5^{+0.4}_{-0.2}$	$4.54^{+0.89}_{-0.78}$	$5.53^{+4.27}_{-2.78}$
A267	0.230	$5.6 \pm 0.1$	$3.23^{+0.82}_{-0.69}$	$4.01^{+3.22}_{-2.07}$
A383	0.188	$4.1 \pm 0.1$	$3.11^{+0.88}_{-0.69}$	$5.44^{+6.55}_{-3.54}$
A520	0.203	$7.9 \pm 0.2$	$5.3^{+3.9}_{-2.6}$	$0.80^{+0.39}_{-0.29}$
A521	0.248	$6.1 \pm 0.1$	$4.58^{+1.00}_{-0.88}$	$2.21^{+1.18}_{-0.86}$
A586	0.171	$7.8^{+1.0}_{-0.8}$	$6.29^{+2.26}_{-1.69}$	$4.77^{+6.13}_{-3.20}$
A963	0.206	$5.6 \pm 0.1$	$4.1^{+1.6}_{-1.0}$	$4.57^{+0.71}_{-0.64}$

Redshifts and temperatures from Aghanim et al. (2012).

cases we use the log-normal distribution, which has a similar shape, and shift the distribution with a location parameter:

$$f_Y(y; \mu, \sigma, \text{loc}) = \frac{1}{(y - \text{loc})\sigma\sqrt{2\pi}} e^{-\frac{[\ln(y - \text{loc}) - \mu]^2}{2\sigma^2}}, \quad (29)$$

with  $\mu$  and  $\sigma$  being the Gaussian parameters of the distribution of  $\log X$  and  $\text{loc}$  is the location parameter. We take the 68% most probable values and the maximum probability of this log-normal PDF to yield the resulting value  $y_{-}^{+\Delta y_1}_{-\Delta y_2}$  of the quantity  $Y$ .

### 3.2.3 Reliability of the results

Our analysis considers samples of 2600 random realisations of each cluster, but some of them happen to have no solution for  $\xi$ , or to have a solution outside the domain established by Eq. (3). These cases are removed from the analysis, leading to considerably smaller samples for some clusters. That is the case for A1914 and A520, for which we are left with only about 640 and 450 realisations, respectively. A possible explanation for such a large fraction of these samples not having a physical solution for  $\xi$  could be the fact that these two clusters are still dynamically active (Markevitch et al. 2005; Barrena et al. 2013), so their virial states are not as close to equilibrium for our method to be applicable. Although not always specified, the size of the samples is apparent in the histograms, where we use a number of bins proportional to it.

### 3.2.4 Evaluating the method: simulation

We tested our method for consistency considering a cluster from  $N$ -body simulation, similar to those of Machado & Lima Neto (2013), in a cosmology with  $\Omega_M = 0.3$ ,  $\Omega_{DE} = 0.7$ ,  $h = 0.72$  and no interaction in the dark sector, so the virial ratio should be very close<sup>1</sup> to  $-0.5$  and interaction compatible with zero. The data for this cluster are  $M_{200} = 18.0 h^{-1}10^{14}M_{\odot}$ ,  $z = 0.0$ ,  $c = 3.0$  and

<sup>1</sup> Some variations can be introduced by the effects of projection translating from simulation to observables.

**Table 4.** Virial ratios, interactions, theoretical virial ratios and departure from equilibrium from the log-normal fits.

Cluster	$\frac{\rho_K}{\rho_W}$	$\xi$	$\left(\frac{\rho_K}{\rho_W}\right)_{th}$	$-\frac{\rho_W}{H\rho_W^2}$
A1835	$-0.71^{+0.06}_{-0.07}$	$-5.04^{+2.11}_{-3.94}$	$-0.74^{+0.05}_{-0.07}$	$-0.07 \pm 0.06$
A1914	$-0.92 \pm 0.04$	$-26.13^{10.63}_{-32.16}$	$-0.93 \pm 0.03$	$-0.02 \pm 0.02$
A2034	$-0.75^{+0.08}_{-0.11}$	$-4.23^{+2.14}_{-12.26}$	$-0.79^{+0.08}_{-0.09}$	$-0.03 \pm 0.06$
A209	$-0.60^{+0.04}_{-0.05}$	$-2.11^{+1.07}_{-1.47}$	$-0.64^{+0.05}_{-0.06}$	$-0.04 \pm 0.07$
A2219	$-0.84 \pm 0.08$	$-9.63^{+4.88}_{-19.95}$	$-0.87 \pm 0.06$	$-0.07 \pm 0.05$
A2261	$-0.56^{+0.06}_{-0.07}$	$-0.93^{+0.98}_{-1.62}$	$-0.60 \pm 0.07$	$-0.03 \pm 0.09$
A2390	$-0.89 \pm 0.06$	$-15.10^{+7.32}_{-25.73}$	$-0.90 \pm 0.05$	$-0.05 \pm 0.04$
A2631	$-0.88^{+0.06}_{-0.07}$	$-12.81^{+6.41}_{-25.37}$	$-0.89 \pm 0.06$	$-0.04 \pm 0.04$
A267	$-0.88^{+0.06}_{-0.07}$	$-10.27^{+5.02}_{-25.68}$	$-0.89 \pm 0.06$	$0.00 \pm 0.04$
A383	$-0.62^{+0.09}_{-0.12}$	$-0.35^{+1.01}_{-3.95}$	$-0.60^{+0.09}_{-0.13}$	$0.05 \pm 0.10$
A520	$-0.94 \pm 0.03$	$-32.52^{+11.78}_{-39.59}$	$-0.94 \pm 0.03$	$0.00 \pm 0.00$
A521	$-0.90 \pm 0.05$	$-14.42^{+6.39}_{-25.26}$	$-0.90 \pm 0.05$	$-0.01 \pm 0.03$
A586	$-0.77 \pm 0.11$	$-4.02^{+3.12}_{-12.90}$	$-0.81^{+0.09}_{-0.10}$	$-0.05 \pm 0.08$
A963	$-0.79^{+0.07}_{-0.09}$	$-5.20^{+2.63}_{-12.89}$	$-0.81 \pm 0.08$	$0.00 \pm 0.05$
TOTAL	—	$-1.61^{+2.23}_{-16.34}$	$-0.78 \pm 0.13$	—

$T_X = 7.3 \pm 0.8$  keV. The uncertainty in the temperature comes from the  $\sigma_X - T_X$  scatter relation (Xue & Wu 2000)

$$\sigma_X = 10^{2.49 \pm 0.02} T_X^{0.65 \pm 0.03}, \quad (30)$$

from which  $T_X$  was computed for a 1D dispersion velocity of  $\sigma_X = 1125$  km/s. Because the observed virial ratio is linear with the temperature, the only source of errors in this case, its histogram for all random realisations produced in our code reflects clearly the uniform distribution assigned to the input temperature. Fitting that uniform distribution we find a virial ratio of  $-0.47 \pm 0.04$  from the central 68% most probable values.

With the analysis of Sec. 3.2.2, for the interaction strength we get  $\xi = -0.05^{+0.54}_{-0.69}$ , therefore compatible with the simulation. The theoretical virial ratio is also in accordance with the classic value,  $\left(\frac{\rho_K}{\rho_W}\right)_{th} = -0.51 \pm 0.05$ , while the departure from equilibrium being  $-0.08 \pm 0.06$  satisfies our condition (7).

### 3.2.5 Presentation of the results

In Figs. 1(a) and 4 we show histograms of the virial ratios and in Fig. 2, of the interaction strength, all obtained for each cluster according to this method. They will be discussed in the following sections, together with their corresponding synthesis Figs. 1(b), 3, 5. We also show in Fig. 6 the synthesis for the departure from equilibrium factors.

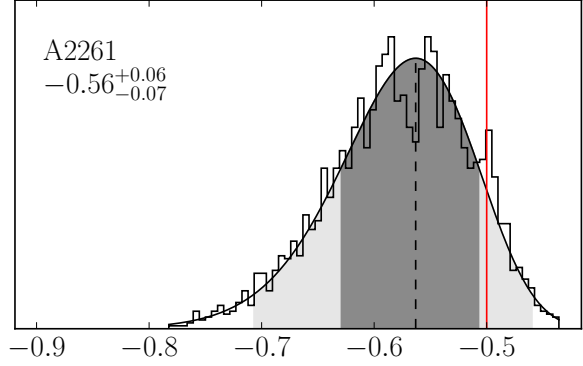
Finally, we summarise these results in Table 4.

## 4 ANALYSIS OF THE RESULTS

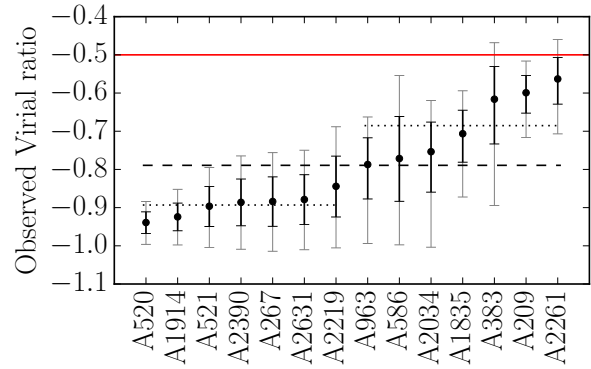
In what follows we discuss the outcome of our analysis starting with the observed virial ratios, their theoretical estimates from combining their departure from equilibrium factors and their interaction strengths.

### 4.1 The observed virial ratios

The observed virial ratio is obtained from applying the method described in Sec. 3.2 to Eq. (14). The histograms of virial ratio produced for each cluster are very similar to what we obtain for their



(a) Observed virial ratio for the cluster A2261 from a sample of 2600 random realisations.  $\frac{\rho_K}{\rho_W} = -0.56^{+0.06}_{-0.07}$ .



(b) Observed virial ratios with error bars indicating 95% and 68% C.L. for all clusters.

**Figure 1.** (a) shows in detail the distribution of observed virial ratios for the cluster A2261 when we apply the Monte Carlo method (Sec. 3.2). The dark and light shaded areas correspond to 68% and 95% C.L. The dashed vertical line indicates the most probable value while the red solid line denotes the classic value. (b) presents the most probable values and confidence levels for each cluster. The grey and black error bars give, respectively, the 95% and 68% C.L. The mean of the most probable values is signaled by the dashed black line. The two dotted lines show the means for the two groups of clusters defined in the text and the solid red line marks the classic value.

theoretical counterparts (see Sec. 4.3). As an example we present in Fig. 1(a) the distribution obtained for the cluster A2261. It represents the histogram distribution of the observed virial ratio obtained from our Monte Carlo sampling of mass, temperature and concentration ranges. Superimposed is the log-normal fit, with light-shaded area corresponding to 95% C.L., and dark-shaded area emphasising 68% C.L. The red vertical line marks the theoretical non-interacting value, while the dashed line gives the most likely value.

We summarise the results of the observed virial ratios with their corresponding asymmetrical errors in Fig. 1(b), where we have shown the theoretical non-interacting virial ratio as a horizontal red line. We have ordered the clusters by increasing observed virial ratio. We keep this order for the rest of the work.

We have represented the mean value for the whole sample with a dashed line. We identify two groups of similar virial ratios separated by the global mean and for each group we represent their means by the dotted lines. The dispersion of the ratios may reflect

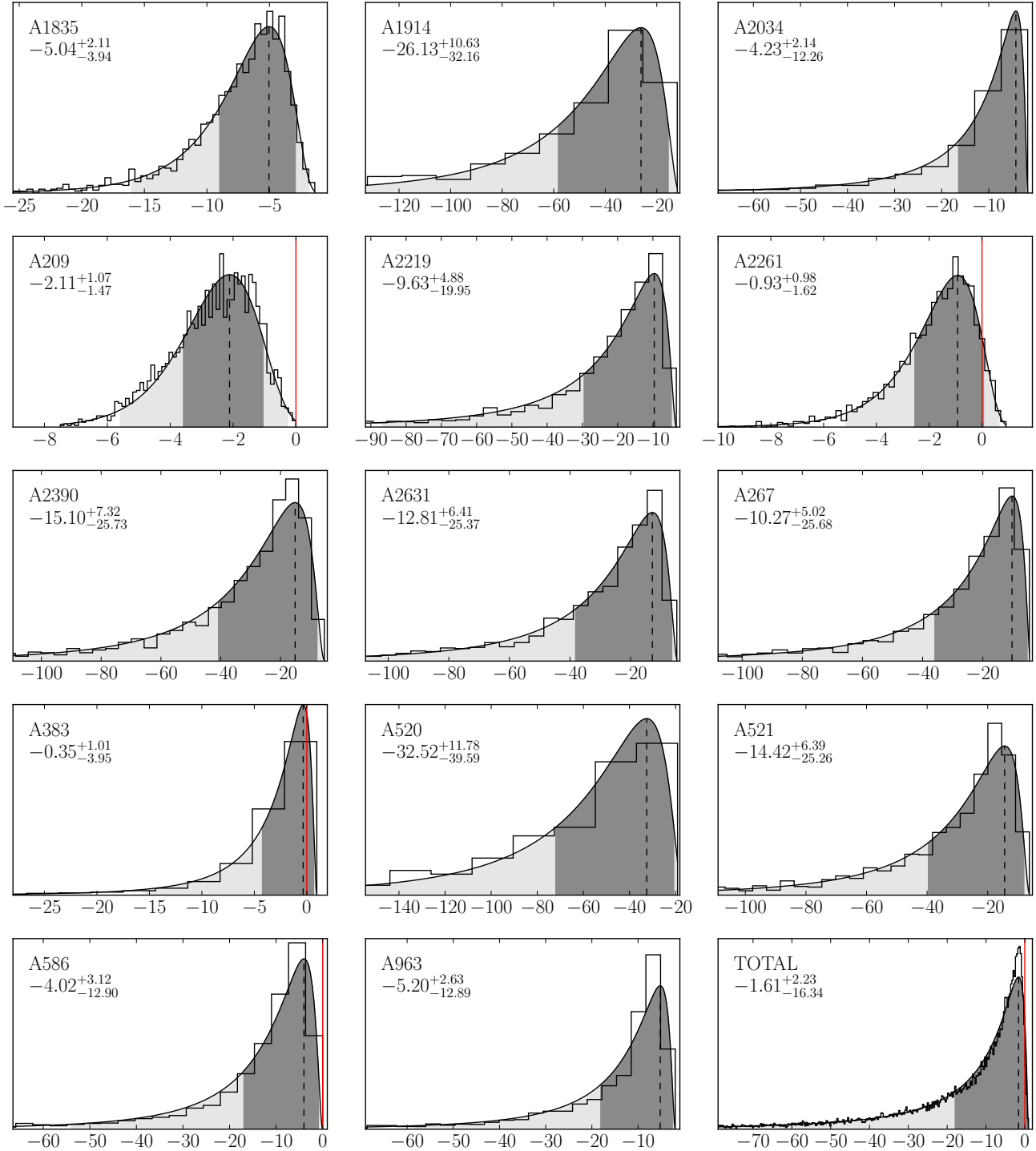


**Figure 2.** Histograms for the distributions of interaction strength with their log-normal fits for each cluster. The lowest rightmost panel presents the cumulated histogram of all the clusters. The dark and light shaded areas mark the 68% and 95% C.I. The dashed lines point the most probable values, while the solid red line, when shown, marks the  $\xi = 0$  position.

the diversity of the equilibrium conditions. However, the first group seems to have less scatter than the second one.

With this robust non-linear treatment of error propagation, all clusters exclude  $-0.5$  at  $1\sigma$ .

## 4.2 The interaction strength

As previously mentioned we solve for  $\xi$  Eq. (6) with the departure from equilibrium term (22) using the Monte Carlo method of Sec. 3.2. Eq. (8) is singular at  $\frac{\rho_\kappa}{\rho_w} = -1$ , which corresponds to  $\xi$  infinite. This is a limitation of our method that we deal with by

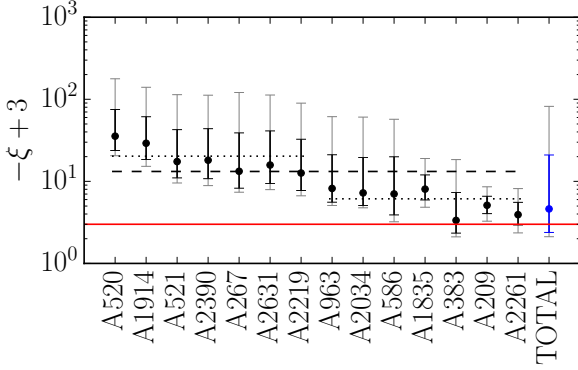


**Figure 3.** Interaction strengths with error bars for each cluster in our sample. The grey and black error bars give, respectively, the 95% and 68% C.L. The most probable value and error bars of the compounded distribution are shown at the right in blue. Again, dotted horizontal lines represent the means for each group of clusters, while the dashed line marks the overall mean. The solid red line marks  $\xi = 0$ . We plot  $-\xi + 3$  rather than  $\xi$  to enable visualization in log scale.

restricting the interaction strength to  $|\xi| \leq 200$  such that the histograms would be legible. Note that this introduces a cut in the histograms of the theoretical virial ratios (Sec. 4.3), which reflects the limitation of our method.

Fig. 2 represents the histograms of interaction strengths for all clusters, the lowest rightmost panel of Fig. 2 displaying the compounded distribution for all the studied clusters. As previously done, the dashed line gives the most probable value, and the light and dark shaded areas correspond to the 95% and 68% C.L., respectively. The red vertical line, when indicated, marks the value of non-interaction.

In Fig. 3 we plot the most probable value of  $-\xi + 3$  for all clusters to keep the log scale, together with the 68% and 95% C.L. corresponding to, respectively, black and grey error bars. The red solid line indicates the  $\xi = 0$  absence of interaction. The mean value for the whole sample is given by the dashed line. Each group previously singled out also present their group mean as dotted lines. Finally, we add the most probable value and error bars of the compounded distribution in blue.

Of the 14 clusters, all of them except A383 and A2261 (marginally) display a  $1\sigma$  detection favouring negative  $\xi$ .

In this model, the interaction strength should be the same for all clusters. The global mean is compatible with 8 of the 14 clusters: A521, A2390, A267, A2631, A2219, A963, A586 and A2034. It gives  $-10.2$ . However, two of the clusters display compatibility with no interaction. This points to problems in our method. Nevertheless, the compounded distribution yields a value for  $\xi = -1.61_{-16.34}^{+2.23}$ , which shows compatibility with no interaction.

### 4.3 The theoretical virial ratios

Armed with the results from the previous section, we compute with Eq. (19) the theoretical virial Ratio that each cluster would have at perfect equilibrium in the presence of interaction. Fig. 4 shows us their corresponding distributions. We keep conventions of light and dark shaded areas representing 95% and 68% C.L., the dashed line for the most probable value and the red solid line to indicate absence of interaction. As those histogram are very similar to the

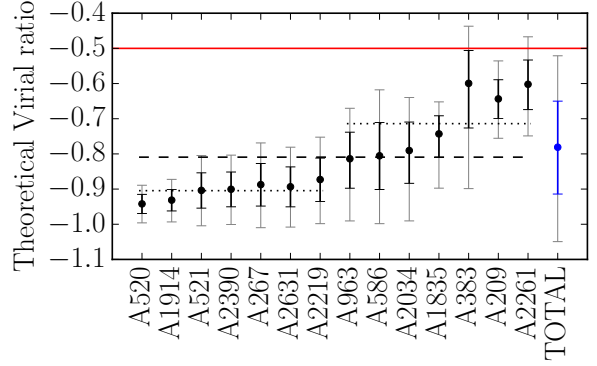


**Figure 5.** Theoretical virial ratios with confidence intervals for each cluster in our sample and for the compounded distribution. Grey and black error bars give, respectively, 95% and 68% C.L. The most probable value and error bars of the compounded distribution are shown at the right in blue. Dotted horizontal lines represent means for each group, while dashed line marks overall mean. The solid red line marks the non-interaction case.

observed ones (Sec. 4.1), the following comments can be applied to both. The reasons for these similarities are discussed in Sec. 4.4. In the same way as in the previous section, we compounded the distributions of theoretical virial ratios for all the clusters, as they should all be equal to a universal value, and show the result in the lowest rightmost panel of Fig. 4.

At this level, all the clusters exclude  $-0.5$  at  $1\sigma$ , which confirms the result from Sec. 4.1 However, 10 out of the 14 clusters present log-normal fits which reflects poorly the underlying distributions: A1914, A2034, A2219, A2390, A2631, A267, A520, A521, A586 and A963. For all of those problematic distributions the log-normal fits break down for virial ratios in the proximity of  $-1$ . This is related to the singularity in Eq. (8). In addition, the compounded theoretical virial ratio points towards a single value of  $-0.78 \pm 0.13$ , which represents a detection at  $2\sigma$ , in contradiction with the results of the previous section. All this indicates a problem with our method. Nevertheless, for the purpose of this work, we keep using the log-normal distribution to produce the most likely values and error bars, as a solution to the above mentioned problems remains out of the scope of this paper.

We plot in Fig. 5 the most probable values of the theoretical virial ratios for all clusters, together with the 68% and 95% C.L. corresponding to, respectively, black and grey error bars. The red solid line indicates the  $-0.5$  classic virial value, in absence of interaction. The mean value for the whole sample is given by the dashed line. We also add the most probable value of the compounded distribution and its error bars in blue.

In the following section, we discuss how the observed and theoretical virial Ratios are so similar.

### 4.4 The departure from equilibrium factors

Eq. (22) with the results of Sec. 4.2 allows us to compute the departure from equilibrium factor for each cluster. The values of this factor relative to their observed virial ratio,

$$-\frac{1}{\left(2 - \frac{\xi}{\bar{\xi}}\right)^2} \frac{\hat{\rho}_w}{H\rho_w} \frac{\rho_K}{\rho_w}, \quad (31)$$



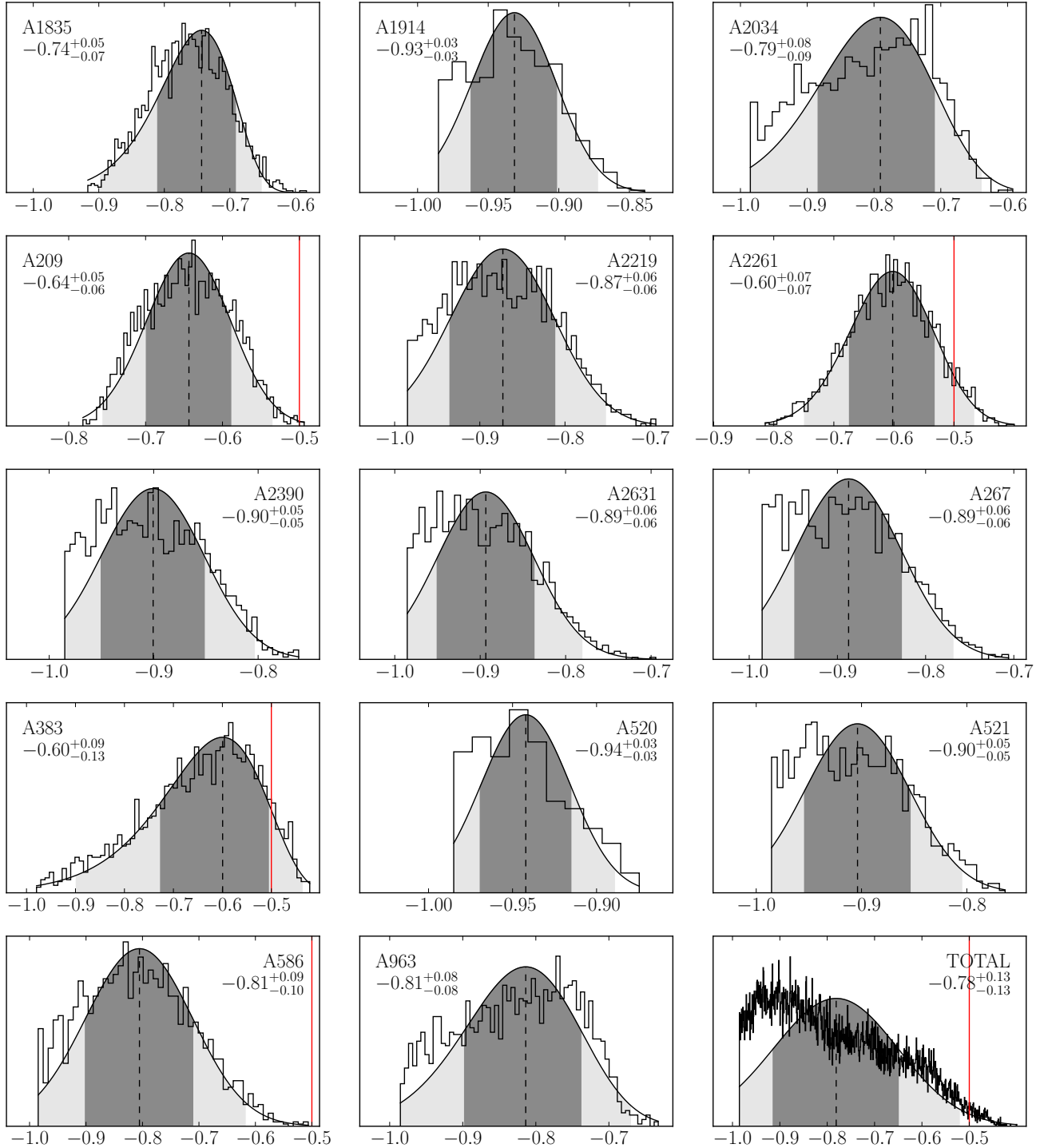


**Figure 4.** Histograms for the distributions of theoretical virial ratios with their log-normal fits for each cluster. The lowest rightmost panel presents the cumulated histogram of all the clusters. The dark and light shaded areas mark the 68% and 95% C.L. The dashed lines point the most probable values, while the solid red line, when shown, marks the position of the no interaction classic virial ratio.

are presented in Fig. 6. Except for A1914, A2219, A2390 and A1835, all those relative departures are compatible with zero. However, the total and group averages cluster around  $-2.7\%$ . We should note as well that A383 is the only cluster with positive departure from equilibrium. For this figure and for numerical reasons, we fit

the distributions for each cluster with uniform distributions so as to evaluate the order of magnitude of those departures and produce the values displayed on Fig. 6. Although not good fits, these uniform distributions enable us to show how small those values are, validating our hypothesis (7). This explains the similarities between the

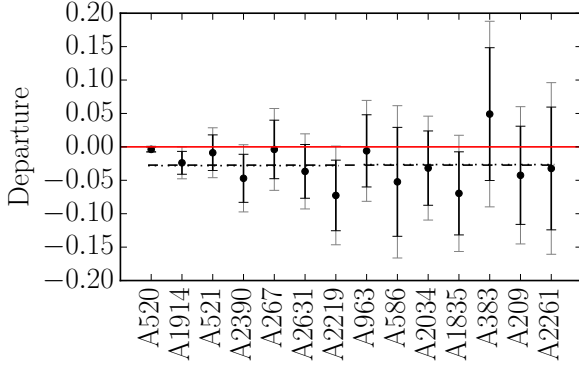


**Figure 6.** Departure from equilibrium factors relative to observed virial ratios with confidence intervals for each cluster in our sample. Grey and black error bars give, respectively, 95% and 68% C.L. Dotted horizontal lines represent means for each group, while dashed line marks overall mean. The solid red line marks the absence of deviation.

observed virial ratios and their theoretical counterparts, as seen in comparing Fig. 1(b) and Fig. 5.

## 5 DISCUSSION AND CONCLUSIONS

We analysed the virial ratios of a set of clusters using a simple model based on the Layzer–Irvine equation (Bertolami et al. 2007; Le Delliou et al. 2007; Bertolami et al. 2008, 2009; Abdalla et al. 2009, 2010; He et al. 2010; Bertolami et al. 2012), using weak-lensing mass profiles and intracluster gas temperatures from optical and X-ray observations (Okabe et al. 2010; Aghanim et al. 2012). Our treatment involved assessing the virial balance of each cluster as well as their equilibrium state, using a Monte Carlo statistical analysis on the data.

Our method enabled us to find mild evidence for an interacting dark sector in the virial balance of those clusters, together with small indications of departure from equilibrium: although a majority of the clusters would accommodate  $\xi = 0$ , the virial ratios point towards a negative interaction. A compounded estimate gives us  $\xi = -1.61^{+2.23}_{-16.34}$ , which is not a detection, but  $\left(\frac{\rho_K}{\rho_W}\right)_{th} = -0.78 \pm 0.13$ , which is a detection at  $2\sigma$ . This tension between the results for the interaction strength and the theoretical virial ratio, the latter being constructed out of the former, adds to the other noted problematic features in our results: despite the scatter in the values of virial ratios, the departure from equilibrium factors remain small, as imposed in our hypotheses; our method contains an unphysical singularity at  $\frac{\rho_K}{\rho_W} = -1$  in Eq. (8). This allows some doubts to be cast in spite of encouraging results and so calls for follow up work which should remove the small departure from equilibrium hypothesis, as well as the singularity we introduced in this work for  $\rho_K = -\rho_W$ .

Most observed clusters appear to be somewhat perturbed systems and are maybe still forming (accreting mass), which is expected in the current standard cosmological scenario. It is natural to treat clusters as out of equilibrium systems as we did in this work. The tension between the results of our measured departure from the classic virial ratio and our measured interaction strength reflects both that our method shows potential but also has room for improvement.

## 6 ACKNOWLEDGEMENTS

The work of M.Le D. has been supported by FAPESP (2011/24089-5) and PNP/DFMA/IF/USP and IFT/UNESP. R.J.F.M. and G.B.L.N thank CAPES for support. G.B.L.N also wish to thank CNPq. E.A. acknowledges FAPESP. Finally, we thank Rubens Machado for his simulation.

## References

- Abdalla E., Abramo L. R. W., Sodr e Jr. L., Wang B., 2009, *Phys. Lett. B*, 673, 107
- Abdalla E., Abramo L. R., de Souza J. C. C., 2010, *PRD*, 82, 023508
- Ade P. A. R. et al. [Planck Collaboration], 2013 [arXiv:1303.5062v2 [astro-ph.CO]]
- Aghanim N. et al. [Planck Collaboration], 2012 [arXiv:1204.2743 [astro-ph.CO]].
- Amendola L., 2000, *PRD*, 62, 043511
- Barrena R., Girardi M., Boschin W., 2013, *MNRAS*, 430, 3453
- Bennett C. L. et al. WMAP Collaboration, 2013, *ApJS*, 208, 20
- Bertolami O., Gil Pedro F., Le Delliou M., 2007, *Phys. Lett. B*, 654, 165
- Bertolami O., Gil Pedro F., Le Delliou M., 2008, *EAS Publ. Ser.*, 30, 161
- Bertolami O., Gil Pedro F., Le Delliou M., 2009, *Gen. Rel. Grav.*, 41, 2839
- Bertolami O., Gil Pedro F., Le Delliou M., 2012, *Gen. Rel. Grav.*, 44, 1073
- He J. -H., Wang B., Abdalla E., Pavon D., 2010, *JCAP*, 1012, 022
- He J. -H., Wang B., Abdalla E., 2011, *PRD*, 83, 063515
- Hinshaw G. et al., WMAP Collaboration, 2013, *ApJS*, 208, 19
- Le Delliou M., Bertolami O., Gil Pedro F., 2007, *AIP Conf. Proc.*, 957, 421
- Machado R. E. G.; Lima Neto G. B., 2013, *MNRAS*, 430, 3249
- Markevitch M., Govoni F., Brunetti G., Jerius D., 2005, *ApJ*, 627, 733
- Moretti A., Gastaldello F., Ettori S., Molendi S., 2011, *A&A*, 528, A.102
- Navarro J. F., Frenk C. S., White S. D. M., 1996, 462, 563
- Okabe N., Masahiro T., Umetsu K., Futamase T., Smith G. P., 2010, *PASJ*, 62, 811
- Peebles P. J. E., 1993, *Principles of physical cosmology*, Princeton Univ. Press, Princeton
- Perlmutter S. et al., 1998, *Nature*, 391, 51
- Pratt G. W., B ohringer H., Croston J. H., Arnaud M., Borgani S., Finoguenov A., Temple R. F., 2007, *A&A*, 461, 71
- Ratra B., Peebles P. J. E., 1988, *Phys. Rev. D*, 37, 3406
- Sympy Development Team, SymPy: Python library for symbolic mathematics, <http://www.sympy.org>
- Tocchini-Valentini D., Amendola L., 2002, *PRD*, 65, 063508
- Vikhlinin A., Markevitch M., Murray S. S., Jones C., Forman W., Van Speybroeck L., 2005, *ApJ*, 628, 655
- Weinberg S., 1989, *Rev. Mod. Phys.*, 61, 1
- Weinberg S., 2008, *Cosmology*, Oxford Univ. Press, Oxford
- Wetterich C., 1988, *Nucl. Phys. B*, 302, 668
- Xue Y. -J., Wu X. -P., 2000, *ApJ*, 538, 65
- Zimdahl W., Pav on D., 2001, *Phys. Lett. B*, 521, 133
- Zimdahl W., Pav on D., 2003, *Gen. Rel. Grav.*, 35, 413
- Zwicky F., 1933, *Helv. Phys. Acta*, 6, 110

Zwicky F., 1937, ApJ, 86, 217